Nano Research

Open Access

Research Article

Enhancement of grain boundary interactions to promote mechanical stability of LNO under deep delithiation conditions

Han Luo[1], Kai Qiu[2], Yang Li[2], Cong Xu[2], Xiaowen Chen[1] ✉, Xinyu Rui[2], Zetian Chen[1], Gaolong Zhu[2] ✉, Xiang Liu[3], Yi Guo[4], Hongkun Pan[3], Yike Gao[2], Chengdong Liang[2], Bin Luo[1], Junwei Yang[1], Defen Zhang[1], and Tiening Tan[2] ✉

[1] *School of New Energy and Materials, Southwest Petroleum University, Chengdu 610000, China*
[2] *Prof. Ouyang Minggao Academician Workstation & Sichuan New Energy Vehicle Innovation Center, Yibin 644000, China*
[3] *School of Material Science and Engineering, Beihang University, Beijing 100191, China*
[4] *School of Vehicle and Mobility, Tsinghua University, Beijing 100084, China*

Cite this article: *Nano Research*, **2026**, *19*, 94907901. https://doi.org/10.26599/NR.2025.94907901

ABSTRACT: Cobalt-free $LiNiO_2$ (LNO) is considered a promising cathode for its high energy density and cost-effectiveness. However, its structural instability under deep delithiation severely limits practical application in next-generation batteries. Herein, we propose a high-valence Mo^{6+} doping strategy to simultaneously improve mechanical robustness and electrochemical stability. By stabilizing intergranular interfaces, this method effectively suppresses mechanical degradation induced by lattice strain under deep delithiation. The modified cathode exhibits exceptional electrochemical performance, achieving a specific capacity of 234 mAh·g^{-1} at 0.1 C with 83.4% retention over 100 cycles at 45 °C in lithium-ion batteries (LIBs). Notably, it maintains comparable efficacy in all-solid-state batteries (ASSBs), delivering 239 mAh·g^{-1} at 0.05 C and 82.8% retention after 300 cycles. Density functional theory (DFT) calculations demonstrate a pronounced rise in oxygen vacancy formation energy, increasing from 1.42 to 3.27 eV. These findings offer valuable insights into overcoming the kinetic performance limitations of cobalt-free LNO under deep delithiation conditions.

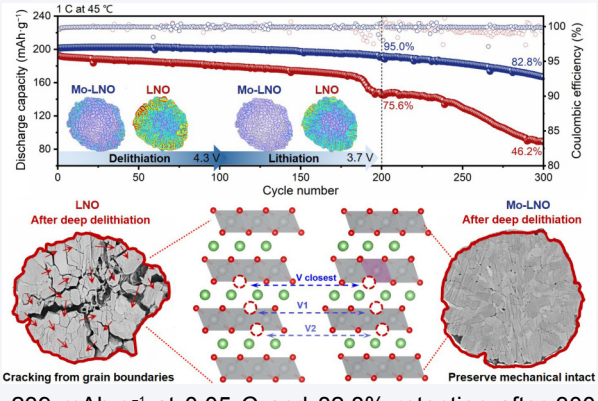

KEYWORDS: cobalt-free cathode, $LiNiO_2$ (LNO), grain boundaries, mechanical stress, deep delithiation

1 Introduction

Lithium-ion batteries (LIBs) are widely regarded as the foremost energy storage technology in electric vehicles and stationary storage systems, owing to their exceptional energy density, robust voltage characteristics, and long-term cycling durability [1–3]. Electric vehicles and energy storage systems represent the primary application domains for LIBs, yet key performance metrics including energy density, safety characteristics, and cost-effectiveness still fail to fully meet the evolving demands of the industry. Nevertheless, the cathode material critically governs the performance characteristics of LIBs. The first commercial $LiCoO_2$ (LCO) batteries were developed and marketed by Sony Corporation of Japan in 1991 [4]. Despite the high theoretical capacity of LCO (274 mAh·g^{-1}), the deliverable capacity is restricted to 140 mAh·g^{-1} under stable delithiation at 4.2 V versus Li^+/Li [5]. Moreover, the long-term viability of LCO in EVs is compromised by the scarcity of cobalt resources worldwide [6, 7]. Consequently, the pursuit of cobalt-free cathodes holds critical importance in driving the sustainable evolution of high-energy layered cathode materials.

$LiNiO_2$ (LNO) has emerged as a critical material in advanced energy storage systems, given its high reversible capacity, resource sustainability, cost competitiveness, and environmental friendliness. However, LNO devoid of the Mn/Co-mediated stabilization, exhibit severe capacity decay and structural deterioration under aggressive delithiation, such as high temperatures or voltages, which may induce an escalation of internal stresses and subsequent collapse of the layered structure [7–11]. Anisotropic unit cells undergo heterogeneous volumetric expansion, which, when severely aggravated, localizes stress and initiates intergranular microcracks

Received: May 21, 2025; **Revised:** July 17, 2025
Accepted: August 6, 2025

✉Address correspondence to Xiaowen Chen, xwchen5188@163.com; Gaolong Zhu, gaolong.zhu@sevc.com.cn; Tiening Tan, tiening.tan@sevc.com.cn

[12]. The propagation of microcracks drastically enhances electrolyte permeability, enlarging the electrode–electrolyte interfacial area and exacerbating Ni^{4+}-involved side reactions. This degradation pathway culminates in the electrochemically inactive rock salt phase [11, 13]. Notably, increasing the operating potential or temperature of LNO for high-energy-density applications could exacerbate oxygen redox activity, thereby undermining the structural integrity of lattice oxygen [14, 15]. Consequently, effectively mitigating particle cracking and crystallographic plane slippage induced by mechanical stress has emerged as a pivotal challenge in the structural design of LNO cathodes.

To mitigate mechanical degradation in cathode materials under high delithiation states, microstructure engineering reinforces structural stability through tailored lattice modulation. While the literature extensively covers strategies to stabilize layered oxides under high voltages, current methods still exhibit pronounced limitations in high-temperature operation [6, 16, 17]. Assessing the structural stability of layered cathodes at elevated temperatures requires rigorous evaluation of key failure mechanisms, such as crystallographic phase transitions, mechanical degradation, and electrode–electrolyte interfacial side reactions. To date, investigations into the structural stability of LNO cathodes at elevated operating temperatures (> 45 °C) have been limited. Solid-state batteries (SSBs), among the most promising energy storage technologies, have attracted significant research interest [18–20]. Moreover, most theoretical studies remain concentrated on their high-temperature performance. Notably, LNO are regarded as a leading candidate for all-solid-state batteries (ASSBs), a status attributed to their exceptional electrochemical properties. Consequently, suppressing mechanical degradation in layered cathodes at elevated temperatures is a pivotal challenge demanding focused research in materials development.

High-valence element doping (e.g., Nb, Ta, W, Mo) exhibits superior efficacy compared to low-valence counterparts in inhibiting particle coarsening within Ni-rich cathodes, effectively preserving structural integrity across extended lithiation temperature ranges—a phenomenon well-documented in previous research [6, 21–23]. However, these advantages are increasingly offset by emerging challenges as nickel content rises. Current doping strategies are inadequate in addressing the propagation of mechanical fractures during deep delithiation and the inherent trade-off between structural stabilization and the Li^+ mobility degradation. Mo^{6+} doping is strategically selected for LNO cathodes based on valence adaptability and atomic dimensions. Its adaptable high valence state stabilizes delithiated structures through cationic ordering, and optimal ionic radius (0.59 Å) comparable to Ni^{3+} (0.56 Å). This dual functionality enables controlled Li-layer expansion for enhanced Li^+ diffusion and minimal lattice distortion during cycling. In contrast, alternative high-valent dopants (W^{6+}: 0.60 Å; Ta^{5+}: 0.64 Å) induce excessive strain, compromising particle integrity under deep delithiation-induced lattice strain during long cycling processes [11, 24, 25]. Herein, we establish high-valence Mo^{6+} doping as an effective strategy for stabilizing LNO under deep delithiation conditions through a grain boundary strengthening mechanism. Our comprehensive analysis reveals that the strengthened Mo–O covalent bonds enhance grain boundary cohesion and significantly improve the cathode's mechanical integrity and structural stability during deep delithiation. Through systematic investigation of electrochemical performance, fundamental physicochemical properties, and cycling durability, we demonstrate how stress relief caused by enhanced grain boundary interactions contributes to remarkable performance enhancement. Furthermore, by integrating electrochemical-mechanical coupling simulations with first-principles calculations, we elucidate the atomic-scale mechanisms governing Mo dopant incorporation and its stabilization effects under elevated temperature operation.

2 Experimental section

2.1 Synthesis of cathode materials

As shown in Fig. S1 in the Electronic Supplementary Material (ESM), Mo-doped LNO (denoted as Mo_x-LNO, where x represents the doping percentage) was synthesized by introducing MoO_3 during the lithiation of the cathode precursor. The mixture included $Ni(OH)_2$ (Sichuan New Energy Vehicle Innovation Centre Co., Ltd.), $LiOH{\cdot}H_2O$ (Yibin Tianyi Lithium Industry Co., Ltd.), and MoO_3 (Klamar), adhering to a molar ratio of $1-x$:1.03:x, where x = 0, 0.002, 0.005, 0.010 for LNO, $Mo_{0.2}$, $Mo_{0.5}$, $Mo_{1.0}$, respectively. The aforementioned mixture was thoroughly homogenized and subsequently calcined in a tube furnace (Crystal) for 10 h at temperatures ranging from 640 to 670 °C while continuously supplying O_2 (99.6% purity), to obtain undoped LNO: LNO-640, LNO-650 (abbreviated as LNO), LNO-660, and LNO-670, respectively; different doping content: $Mo_{0.2}$-650, $Mo_{0.5}$-650 (denoted as Mo-LNO), $Mo_{1.0}$-650, respectively; and different sintering temperatures (0.5 mol%): $Mo_{0.5}$-640, $Mo_{0.5}$-650 (denoted as Mo-LNO), and $Mo_{0.5}$-660, respectively. Based on the preliminary electrochemical cycling data, Mo content of 0.5 mol% and 650 °C of sintering temperature have been identified as optimal (Fig. S4 in the ESM).

2.2 Materials characterization

To investigate the cross-sectional morphology of materials, electrodes were prepared and sectioned using a cross-sectional polisher (CP, Hitachi). Scanning electron microscopy (SEM, Hitachi) and energy dispersive spectroscopy (EDS, Oxford) were employed to analyze the morphologies and elemental distributions of the prepared cathode powders and cycled electrodes. The mechanical failure resistance of cathode particles was evaluated using the single-particle mechanical property testing system (Initial Energy Science & Technology (Xiamen) Co.,Ltd.) controlled by displacement, pressure and software integration. The crystal structures of the cathode materials were examined through X-ray diffraction analysis (XRD, Rigaku) utilizing a Cu Kα radiation source. XRD data were collected over a 2θ range of 5° to 90° with a step width of 0.01°, and the data were subsequently refined utilizing the Rietveld refinement program GSAS-II. Raman spectra (Renishaw inVia Raman microscope) were collected with ten scans (30 s per scan), 0.5 mW, 513 nm laser and ×50 optical magnification. The chemical compositions and ion species of materials were assessed using X-ray photoelectron spectroscopy (XPS, Thermo Fisher Scientific). Specimen preparation for transmission electron microscopy (TEM) analysis was conducted using focused ion beam scanning electron microscopy (FIB-SEM, Thermo Fisher Scientific). The micro-layered structure was characterized by high-resolution transmission electron microscopy (HR-TEM, Thermo Fisher Scientific). For *in situ* XRD testing during the charging and discharging processes, a specially designed electrochemical reaction cell featuring a beryllium window to

facilitate X-ray penetration was assembled. *In situ* XRD patterns were collected every 20 min within a 2θ range of 5° to 90° and a voltage range of 2.8 to 4.3 V (vs. Li^+/Li) at 0.1 C. Structural evolution was examined by differential scanning calorimetry (DSC) with temperature ranging from room temperature to 500 °C.

2.3 Electrochemical tests

As illustrated in Fig. S2 in the ESM, coin-type half-cells were prepared for subsequent electrochemical tests. The cathodes were fabricated by mixing a cathode material, polyvinylidene fluoride (PVDF), and acetylene black in a mass ratio of 80:10:10 in N-methyl-2-pyrrolidone (NMP). The resulting slurries were coated onto Al foils with an active material loading of 4–5 mg·cm^{-2} and then vacuum dried at 85 °C. Then, the electrodes were roll-pressed and punched into small discs with an area of ~ 113 mm^2. Using Li metal (Canrd) as the anode, single-sided ceramic diaphragms (Canrd) as the separator, and ternary electrolyte (KLD-1230C, Canrd), CR2032-type coin cells were assembled in an Ar-filled glovebox. The coin-type half-cells were activated for 3 cycles at 0.1 C, after which the charge/discharge cycling tests (100 cycles @1 C) were evaluated on a LANDt instruments (Boling) at 45 and 25 °C, with a voltage range of 2.8 to 4.3 V. The galvanostatic intermittent titration technique (GITT) measurements were performed by applying current pulses at 0.3 C for 10 min duration, followed by 30 min relaxation intervals. These data enabled quantitative determination of Li^+ diffusion coefficient (D_{Li^+}). Electrochemical impedance spectroscopy (EIS) was conducted on an electrochemical workstation (Metrohm) using a perturbation amplitude of 5 mV across a frequency range of 0.01 Hz to 1 MHz at 45 °C.

A composite cathode was prepared by thoroughly mixing the active material, sulfide solid electrolyte ($Li_{5.4}PS_{4.4}Cl_{1.6}$, Sichuan New Energy Vehicle Innovation Centre Co., Ltd.), and vapor-grown carbon fiber (VGCF, Canrd) conductive additive in a 70:30:3 weight ratio in an agate mortar. A cell was assembled using 85 mg of SE, 12 mg of the composite cathode material, and a lithium-indium alloy anode (composed of a ϕ10 mm indium foil and a ϕ6 mm lithium foil). The assembled ASSBs were activated at 0.05 C, after which the charge/discharge cycling tests (300 cycles @1 C) were evaluated on a LANDt instruments (Boling) at 45 °C, with a voltage range of 2.1 to 3.7 V. EIS was conducted on an electrochemical workstation (Metrohm) using a perturbation amplitude of 10 mV across a frequency range of 0.01 Hz to 10^7 Hz at 45 °C.

2.4 Simulation and calculation methods

COMSOL multiphysics was employed to develop an electrochemical–mechanical model aimed to simulate the mechanical stress induced during the delithiation process of LNO. The model was developed based on actual cross-sectional images of cathodes, and the electric stress coupling simulation was conducted utilizing image recognition technology alongside fine grid discretization. The boundary condition for secondary particles was established as a compacted fixed state, while the internal primary particles were designated as being in a roller-supported state. First-principles calculations were conducted utilizing the Cambridge Serial Total Energy Package (CASTEP) code within the density functional theory (DFT) framework [26]. The on-the-fly generation of potentials (OTFG ultrasoft) method and the generalized gradient approximation (GGA) of Perdew–Burke–Ernzerhof (PBE) form were employed to exchange the relevant energy generalization. Recognizing the challenges in accurately characterizing localized d-orbital electrons using the GGA method, the GGA+U approach was adopted to calculate the structural and thermodynamic properties of transition metal (TM) oxides [27]. Common values of 3.5 and 6.0 eV were selected for Mo and Ni, respectively. Meanwhile, the van der Waals correction based on Grimme's DFT-D model was incorporated [28]. The simulations were terminated when the total energy converged to within 10^{-5} eV·atom^{-1}, with stress values below 0.05 GPa, forces less than 0.03 eV·Å^{-1}, and displacements under 0.001 Å. The plane-wave cutoff energy was set to 550 eV. K-point meshes of 2 × 2 × 1 and 4 × 4 × 2 were utilized for structural optimization and density of states (DOS) calculations, respectively. The full linear synchronous transit (LST)/quadratic synchronous transit (QST) method was employed to calculate the diffusion energy barrier of Li^+ migrating between octahedral sites during the charging process, specifically performing LST initially and then repeating conjugate gradient minimization and QST maximization until the transition state was identified [29].

3 Results and discussion

The influence of operational temperatures on the cycling stability of Mo-LNO and LNO is illustrated in Fig. 1(a). Exhilaratingly, Mo-LNO demonstrates a greater gap of cycling performance with a 14.7% enhancement under the high temperature of 45 °C. Specifically, the capacity retention after 100 cycles of Mo-LNO is 83.4% and 91.7% at 45 and 25 °C, respectively, whereas that of LNO is 68.7% and 82.9%, respectively. The cycling performance and discharge capacity featuring undoped and Mo doped LNO at 45 °C are presented in Figs. S3–S5 in the ESM. Mo-LNO exhibits a high specific capacity of 234 mAh·g^{-1} at 0.1 C, which is comparable to that of LNO, emerging as the superior cathode among those evaluated due to the trade-off between reversible capacity and cycling stability.

As depicted in Figs. 1(b) and 1(c), the evolution of the charge and discharge curves indicates that LNO experiences a significant voltage decline and a considerable capacity loss during high-temperature cycling when compared to Mo-LNO. As the cycle progresses, the slope of the discharge plateau increases until the plateau features disappear. The differential capacity (dQ/dV) curves for Mo-LNO and LNO during the discharge process at 45 °C are shown in Figs. 1(d) and 1(e). The reduction peaks in dQ/dV profiles directly reflect the thermodynamic phase transitions and kinetic behavior during lithiation, with the reversibility of these transitions fundamentally determining the electrode's capacity retention [6, 30, 31]. Remarkably, unlike the peak for LNO, the reduction peak (> 4.1 V) for Mo-LNO remains well-defined even after 100 cycles, as further corroborated by the observed attenuation of the voltage plateau (Figs. 1(b) and 1(c)). Hence, high-valence Mo^{6+} doping effectively suppresses both voltage decay and capacity fade of LNO during extended high-temperature cycling, which is achieved by suppressing the accumulation of lattice strain in the deeply delithiated H3 phase during repeated cycling, thereby preventing irreversible structural damage.

In terms of rate performance, Mo-LNO demonstrates a superior high-rate capability at 45 °C (Fig. S6(a) in the ESM), possessing a capacity of 126.7 mAh·g^{-1} at 10 C compared to that of LNO (117.3 mAh·g^{-1}), this disparity is even more pronounced than that observed at 25 °C (Fig. S6(b) in the ESM). The observed difference

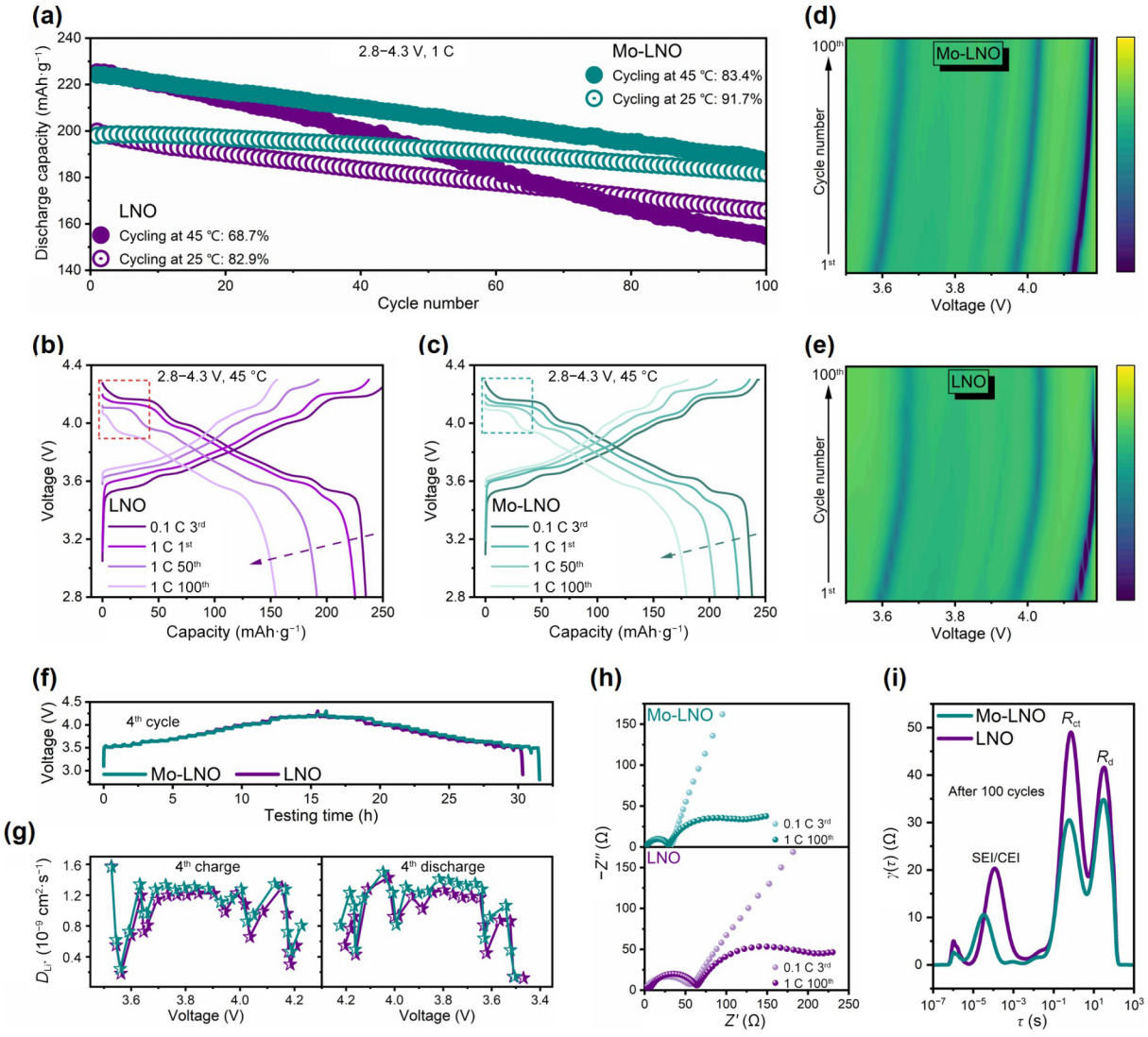

Figure 1 Electrochemical performances of Mo-LNO and LNO cathodes in half cells. (a) Cycling performances of half cells featuring Mo-LNO and LNO at 45 and 25 °C. Charge–discharge curves of (b) Mo-LNO and (c) LNO at different cycles at 45 °C. The d*Q*/d*V* curves of (d) Mo-LNO and (e) LNO at 45 °C. (f) GITT curves and (g) D_{Li^+} of Mo-LNO and LNO for the 4th cycle number after activation at the same charge–discharge period at 45 °C. (h) Impedance spectra evolution of Mo-LNO and LNO at activation of the third cycling and after 100 cycles at 45 °C. (i) The DRT results after 100 cycles at 45 °C.

in cathode capacity stability at 0.1 C between 45 and 25 °C primarily stems from temperature-dependent electrode kinetics. This phenomenon can be quantitatively explained by the Arrhenius relationship for Li^+ diffusion. Elevated temperature (45 °C) accelerates the transport of Li^+ in the cathode phase and interface, enabling faster electrode equilibration during the activation stage. Specifically, Li^+ migration through the crystalline lattice is significantly accelerated at 45 °C, which directly improves rate charge–discharge performance due to enhanced ionic conductivity and reduced R_{ct}. The elevated temperature of 45 °C provides additional thermodynamic driving force that enables deeper Li^+ extraction (H2-H3 phase transition), and high-temperature environment allows Mo^{6+} doping to more obviously suppress irreversible collapse of the H3 phase structure, thereby restoring Li^+ diffusion pathways.

The GITT curves for Mo-LNO and LNO are presented in Fig. 1(f), offering insights into the kinetic characteristics of the solid phase. The current pulse profile and the calculated D_{Li^+} following activation are illustrated in Fig. 1(g). The D_{Li^+} values of Mo-LNO are significantly greater than those of LNO during both the charging and discharging processes. This kinetic improvement confirms that Mo^{6+} doping effectively facilitates Li^+ transport during deep intercalation/deintercalation at elevated temperature. To elucidate the impact of Mo doping on Li^+ transport kinetics in LNO electrodes, we employed EIS coupled with distribution of relaxation times (DRT) analysis. As demonstrated in Fig. 1(h), LNO exhibits high initial Li^+ diffusion resistance due to underdeveloped ionic conduction pathways while Mo-LNO maintains a reduced impedance level during whole process. Interfacial impedance initially decreases due to stable solid electrolyte interphase (SEI) formation but subsequently increases as oxygen redox reactions trigger interfacial degradation. DRT deconvolution (Fig. 1(i)) identifies three critical processes characterized by relaxation times (τ): SEI/cathode electrolyte interface (CEI) film resistance, charge transfer resistance (R_{ct}), and diffusion resistance (R_d). Notably, Mo-LNO suppresses the dramatic impedance growth observed in pristine LNO, as evidenced by a 37.9% decrease in R_{ct} and a 16.8% decrease in R_d, confirming its superior interfacial stabilization effect.

The charge transfer resistance at the cathode–electrolyte interface increases more rapidly in LNO, indicating poorer electronic and ionic conductivity, likely attributable to adverse phase transitions that cause particle cracking and disrupt electronic and ionic transport pathways [32].

The electrochemical performance of the modified Ni-rich cathodes is summarized in Table S1 in the ESM [11, 13, 25, 33–39]. Remarkably, the Mo-LNO developed in this work demonstrates a higher discharge capacity than most of the other cathodes at elevated rates and exhibits cycling stability comparable to that of NCM83. This enhancement can be attributed to strain relief and lattice oxygen stability resulting from the optimal doping of Mo in LNO cathodes, which aids in preventing structural collapse during deep delithiation, thereby enhancing electrochemical stability at elevated temperatures.

To investigate the effects of Mo doping on the morphology of cathode materials, Mo was incorporated at concentrations ranging from 0.2 mol% to 1 mol% (Fig. 2(a) and Fig. S7(a) in the ESM). Subsequently, the Mo-LNO was analyzed using energy EDS to assess the distribution of elements (Fig. S7(b) in the ESM). The results indicate that Ni (blue), O (green), and particularly Mo (purple) are distributed throughout the Mo-LNO cathode materials, which suggests that Mo^{6+} is incorporated into the LNO cathode material resulting in a solution rather than a distinct second phase. Furthermore, the Mo doping strategy effectively inhibited the growth of primary particles compared to undoped LNO cathodes (Fig. 2(b) and Fig. S8 in the ESM). As illustrated in Figs. 2(c)–2(e), the refinement of primary particles with submicron particle size in Mo-LNO compared to LNO increases the fraction of particle boundaries per unit area, which helps to alter the crack propagation path and dissipate strain energy [40–42]. Additionally, the numerous interparticle boundaries create shorter and more efficient diffusion paths for Li^+, facilitating significantly faster Li^+ migration through the relatively loose atomic arrangements at these boundaries compared to the bulk phase [43].

As shown in Fig. 2(f), the mechanical strength of the cathodes is

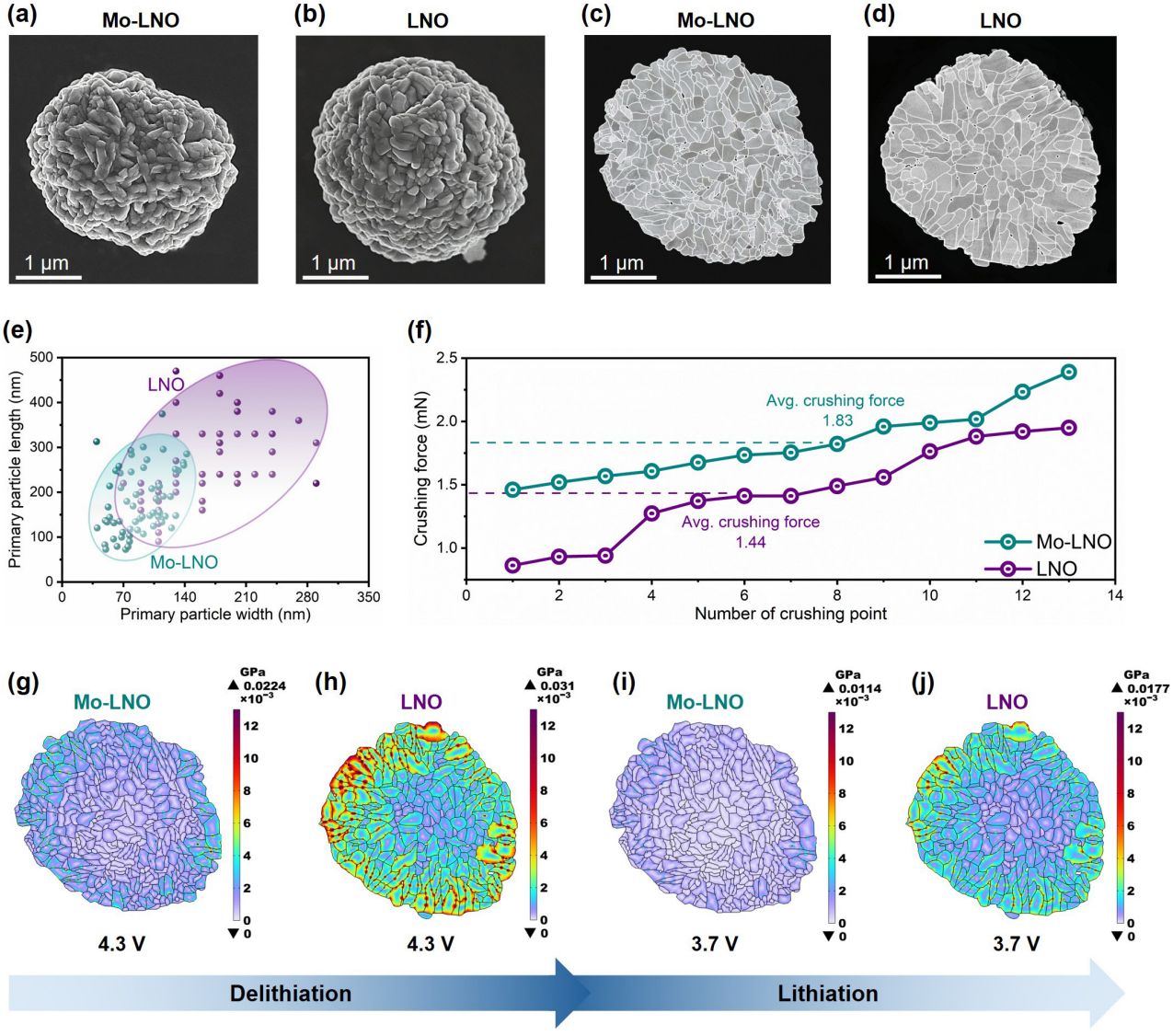

Figure 2 Comparison of primary particle morphologies and mechanical stability. SEM images of (a) Mo-LNO and (b) LNO. Cross-sectional SEM images of (c) Mo-LNO and (d) LNO. (e) Measured length and width of primary particles in Mo-LNO and LNO. (f) Comparison of crushing force for Mo-LNO and LNO. The stress distribution of (g) Mo-LNO and (h) LNO at the end of charge, as well as (i) Mo-LNO and (j) LNO at the end of discharge through electrochemical-mechanical simulation.

evaluated using single-particle mechanical performance testing. Mo-LNO demonstrates improved crushing force with a 27.1% enhancement compared to LNO. This finding suggests that Mo-LNO possesses superior mechanical properties, enhancing its ability to withstand microcracks induced by strain during battery cycling at elevated temperature. The simulation model for single-particle mechanical failure provides a comprehensive analysis of the differences in mechanical stress distributions between Mo-LNO and LNO under 1 C charge–discharge conditions. At the end of both the charge and discharge processes, stress distribution is predominantly concentrated at the exterior of particles, as depicted in Figs. 2(g)–2(j). Notably, the stress in external particles experienced by Mo-LNO is significantly lower than that of LNO particles, which diminishes the mechanical strain accumulation that occurs in the cathode during Li^+ extraction and insertion. Hence, Mo doping enhances both the intrinsic mechanical strength of LNO cathode particles and their resistance to electrochemical–mechanical strain during cycling. This dual effect will simultaneously mitigate particle fracture, ultimately improving battery cycle life and safety.

The phase identification and structural characterization of Mo-LNO and LNO were evaluated using XRD techniques. As shown in Fig. S9 in the ESM, Mo-LNO exhibits a single-phase structure with diffraction peaks that closely resemble those of LNO, indicating a layered hexagonal configuration corresponding to the $R\bar{3}m$-$NaFeO_2$ structure within its respective space group. Additionally, the shift in the (003) peak of Mo-LNO suggests that the expansion of lattice parameters is beneficial for Li^+ mobility. According to the Scherrer equation, the full width at half maximum (FWHM) is inversely related to grain size. The substantial broadening observed in the (003) diffraction peak upon Mo doping confirms a significant refinement of the grain size [44]. Furthermore, the observation of peaks splitting at (006)/(012) and (018)/(110) further indicates a high degree of ordering in the crystal structures of Mo-LNO and LNO. The degree of Li/Ni cation mixing in Mo-LNO is measured at 2.38%, compared to 1.85% in LNO, as estimated from the corresponding Rietveld refinement data (Figs. 3(a) and 3(b), and Table S2 in the ESM). Additionally, the Mo-doped cathodes confirm that the ordered layered structure is preserved (Figs. S10 and S11 in the ESM), and cation mixing increases with higher Mo

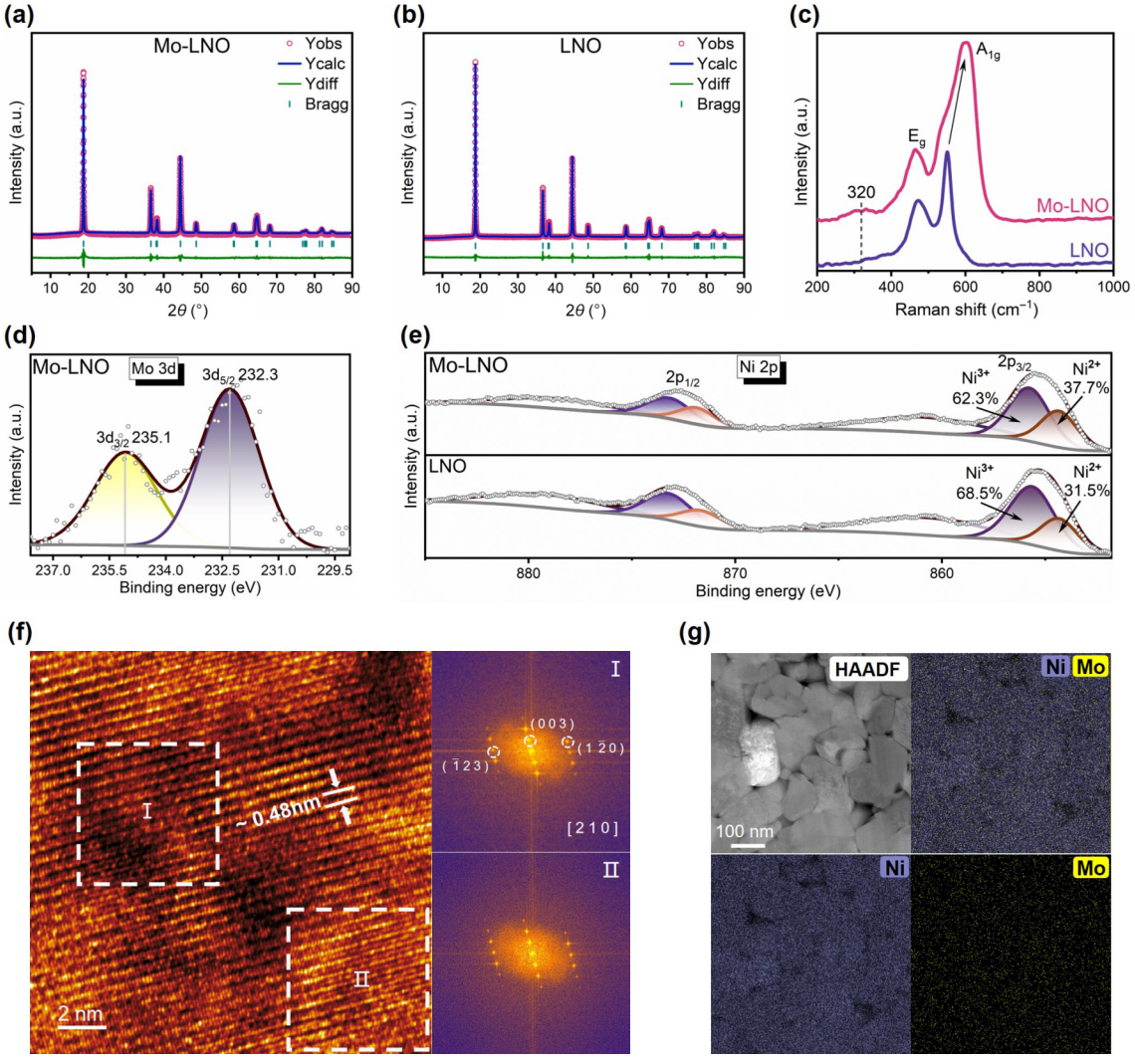

Figure 3 Comparison of pristine structures of Mo-LNO and LNO cathodes. Rietveld refinement of the XRD data for (a) Mo-LNO and (b) LNO cathodes. (c) Raman spectra and peak shift of A_{1g}. (d) Mo 3d spectra of Mo-LNO and (e) Ni 2p spectra of Mo-LNO and LNO. (f) The HRTEM image on the central areas of Mo-LNO particles and the FFT patterns of the selected dark and bright region. (g) The HAADF-STEM image of Mo-LNO based on FIB cutting and corresponding EDS mapping analysis of Ni and Mo.

content (Table S2 in the ESM). The substitution of Mo at the TM site leads to a reduction of Jahn-Teller active Ni^{3+} to Ni^{2+}, which is necessary to maintain charge neutrality, while also alleviating the presence of high-active Ni^{4+} during the delithiation process due to the charge compensation effect of high valence [13, 45, 46].

The thermal runaway (TR) temperature is fundamentally governed by the metal–oxygen (M–O) bond strength, which can be quantitatively assessed through Raman spectroscopy. As shown in Fig. 3(c), Mo-LNO reveals a distinct peak at 320 cm^{-1}, corresponding to Mo–O–Ni bending vibrations that confirm covalent bond existence. This Mo doping-induced modification significantly enhances the M–O bond strength, as evidenced by the characteristic blue shift of the A_{1g} mode (NiO_6 octahedral vibration) in the Raman spectrum. The strengthened bonding network directly correlates with the elevated DSC peak temperature, inferring improved thermal stability [47].

The composition and valence states of the elements present in the pristine Mo-LNO and LNO cathodes were analyzed using XPS. The presence of Mo–O covalent bonds is confirmed in Fig. 3(d), with binding energy values of approximately 232.3 and 235.1 eV, which correspond to the oxidation states of MoO_3 (Mo $3d_{5/2}$ and Mo $3d_{3/2}$, respectively). As shown in Fig. 3(e) and Fig. S12 in the ESM, the Ni 2p spectra of Mo-doped samples ($Mo_{0.2}$-650, Mo-LNO, and $Mo_{1.0}$-650) exhibit significantly higher Ni^{2+}/Ni^{3+} ratios in sequence compared to pristine LNO, demonstrating improved Li^+/Ni^{2+} cation mixing. This conclusion is further supported by XRD Rietveld refinement data (Table S2 in the ESM). The stabilized cationic configuration in Mo-LNO cathodes offers dual benefits of enhanced structural integrity during deep delithiation and facilitated reversible lattice oxygen redox [48, 49].

As shown in Fig. 3(f), the HR-TEM images of Mo-doped primary particles reveal local structural features at the atomic resolution. The fast Fourier transform (FFT) of selected dark and bright regions (Regions I and II) display distinct diffraction spots without any streaks. This observation indicates a high degree of crystallinity along the [210] direction, thereby confirming that Mo-LNO has been successfully integrated into a layered LNO structure characterized by the space group $R\bar{3}m$. The high-angle annular dark field scanning transmission electron microscopy (HAADF-STEM) observations and corresponding elemental mapping in Fig. 3(g) show that both Ni (blue) and Mo (yellow) are distributed within the Mo-LNO cathode materials. Furthermore, quantitative EDS line profiling exhibits Mo enrichment at grain boundaries compared to grain interiors (Fig. S13 in the ESM), confirming that the Mo^{6+} is incorporated into grain boundaries of LNO matrix.

As displayed in Figs. 4(a) and 4(b), *in situ* XRD testing was conducted during charging and discharging processes of Mo-LNO and LNO cathodes and aimed to validate the influence of Mo doping on mitigating irreversible structural distortions. During the extraction of Li^+, a shift of the (003) peak toward a lower angle was observed in low-voltage regions, which is attributed to the increased electrostatic repulsion between neighboring oxygen planes during charging. Starting at approximately 3.7 V, the (003) peak exhibits a shift towards a higher angle, signifying a contraction of the *c*-axis at elevated high state of charge (SOC), which is accompanied by a decrease in unit-cell volume. The contraction mechanism during deep charging can be attributed to phase transformations associated with the "H1-H2-H3" processes, in addition to the localized "lattice collapse" in layered cathodes at high SOC [50]. Additionally, Mo-LNO exhibits a smaller shift of the (003) peak (2θ = 0.88°) in comparison with LNO (2θ = 0.98°), highlighting the enhanced electrochemical reversibility of Mo-LNO cathode.

The critical relationship between structural degradation and electrochemical stability is examined through SEM analysis of cathodes after 100 cycles at 45 and 25 °C. As demonstrated in Fig. 4(c) and Fig. S14 in the ESM, LNO first cracks from grain boundaries and exhibits significant thickening and widespread intergranular microcracks (45 °C), thus most of the secondary particles are fragmented into several pieces. Long and thick microcracks extend to the surfaces of the cathode particles, creating pathways for the liquid electrolyte to infiltrate the interior of the particles. Even at 25 °C, LNO exhibits a tendency to develop microcracks, compromising their long-term stability, whereas Mo-LNO cathodes preserve mechanical intact (Fig. S15 in the ESM). Notably, Mo-LNO maintains its capacity without any visible intergranular microcracks after identical high temperature cycles, effectively protecting interior particles from direct exposure to the electrolyte.

As shown in Fig. 4(d), the XPS peaks associated with F 1s and P 2p after 100 cycles at 45 °C further confirm the degree of structural degradation, with interfacial side reaction products $Li_xPO_yF_z$ and LiF present on both cathode surfaces. The $Li_xPO_yF_z$ concentration decreases from 38.1% (LNO) to 31.6% (Mo-LNO) in the P 2p spectrum, reflecting reduced parasitic reactions. This corresponds to increased contact area between LNO cathodes and electrolytes, which intensified parasitic reactions throughout the cathodes. These findings demonstrate that Mo-LNO effectively suppresses cathode-electrolyte harmful interactions and mitigates degradation through stabilized interface formation [51, 52].

To assess the compatibility of Mo-LNO cathodes with solid-state systems, long-term cycling tests in ASSBs at 45 °C are conducted. As shown in Fig. 5(a), cells were cycled at 1 C and a cut-off voltage of 3.7 V vs. Li-In (equivalent to 4.3 V vs. Li^+/Li), revealing stark performance differences: After 300 cycles, LNO retained only 46.2% capacity, while Mo-LNO maintained 82.8% capacity retention under identical conditions of 45 °C. The enhanced cycling stability of Mo-LNO arises from mechanical rigidity of solid electrolyte synergized with grain-boundary stabilization effect of Mo to simultaneously prevent particle fracture and electrolyte penetration, meanwhile the elevated temperature provides thermodynamic compensation for the solid electrolyte's intrinsic low ionic conductivity [18].

The d*Q*/d*V* profiles of Mo-LNO and LNO cathodes during the H2-H3 phase transition are shown in Fig. 5(b) (full voltage range in Fig. S16 in the ESM). The H2-H3 transition near charge completion dominates the total capacity contribution in Ni-rich cathodes. Hence, Mo doping effectively delays and suppresses this phase transition, as evidenced by the shifted peak position in d*Q*/d*V* curves, which reduces the kinetic barrier for Li^+ intercalation/deintercalation, thereby enhancing electrochemical reversibility [6, 30].

As shown in Figs. 5(c) and 5(d), to evaluate the enhanced rate capability and cycling stability of Mo-LNO in ASSBs, comparative electrochemical testing was conducted at 45 °C across multiple current densities. Mo-LNO demonstrates superior performance, delivering discharge capacities of 203.5 $mAh{\cdot}g^{-1}$ (1 C), 187.7 $mAh{\cdot}g^{-1}$ (2 C), and 161.4 $mAh{\cdot}g^{-1}$ (5 C), while LNO retains only 181.4, 165.1, and 142.5 $mAh{\cdot}g^{-1}$ at corresponding rates. To assess interfacial stability in ASSBs, EIS was performed on both Mo-LNO and LNO electrodes during the initial 0.05 C activation cycle

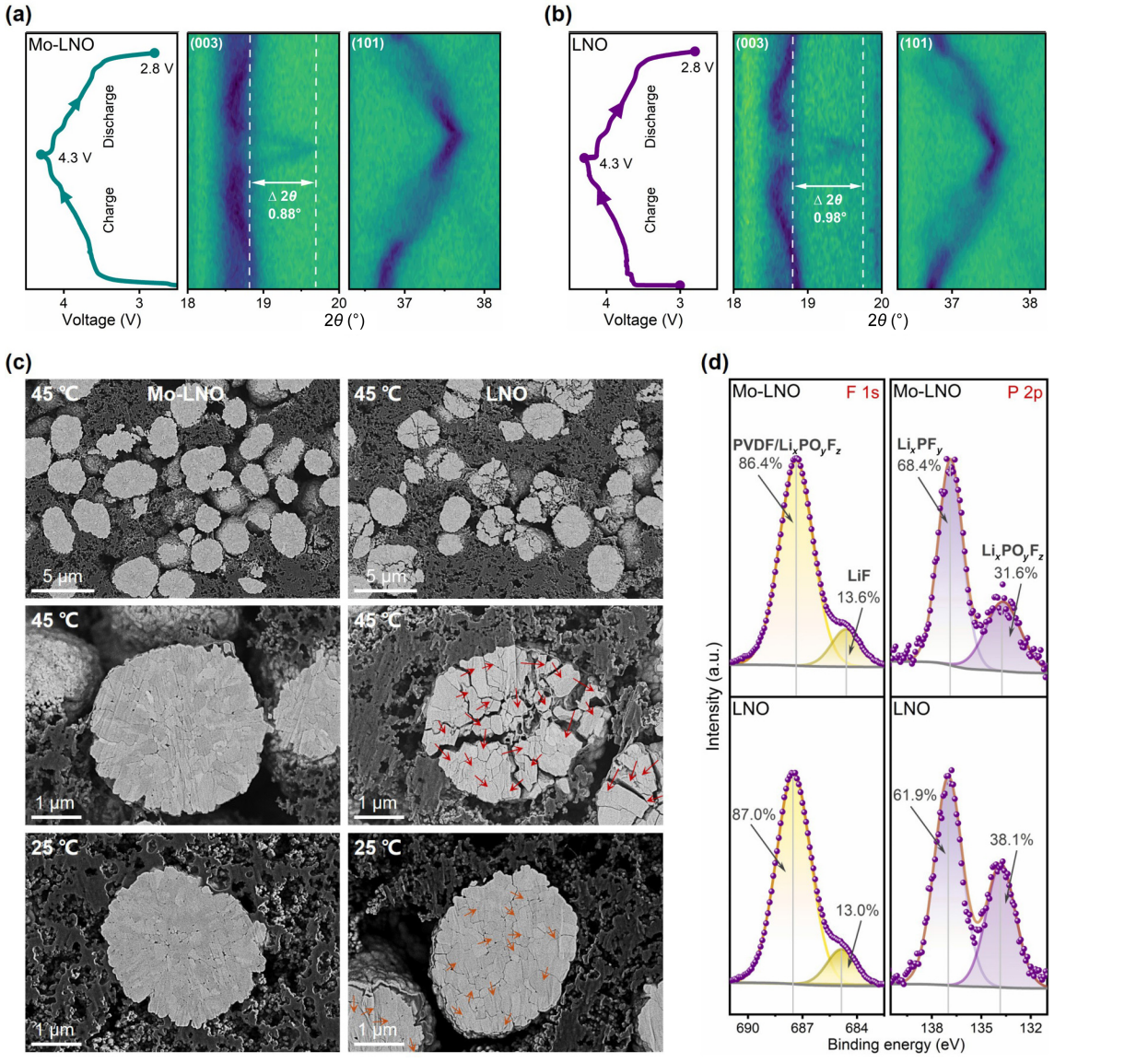

Figure 4 Microstructural durability of Mo-LNO and LNO cathodes. The initial charge–discharge curves and the corresponding *in situ* XRD patterns of (a) Mo-LNO and (b) LNO. (c) Cross-sectional SEM images of electrodes after 100 cycles at 1 C. (d) F 1s and P 2p spectra of electrodes after 100 cycles at 1 C under 45 °C.

and after 100 cycles at 45 °C (Fig. S17 in the ESM). The Mo-LNO electrode demonstrated superior interfacial stability, exhibiting significantly reduced Rohm (3.1 Ω vs. LNO's 7.2 Ω) and Rint (0.97 Ω vs. LNO's 1.5 Ω) after cycling. These results directly correlate with Mo doping's ability to strengthen grain boundaries and stabilize the electrode–electrolyte interface, thereby minimizing degradation during extended cycling.

As depicted in Fig. 5(e), DSC analysis of fully charged cathodes reveals enhanced thermal stability in Mo-LNO compared to pristine LNO. The charged Mo-LNO cathode exhibits a higher exothermic peak temperature (ΔT = +2.6 °C) with reduced heat generation being approximately 83.5% that of LNO cathode, indicating enhancement of thermal stability and safety characteristic.

Through the application of DFT calculations, the optimal Mo doping sites within the LNO cathode are identified. As shown in Fig. S18 in the ESM, the formation energy associated with Mo occupying in Ni sites is lower than that in Li sites. This outcome signifies that Mo–O bonds substituting Ni–O bonds represent the lowest energy configuration, and subsequent models are developed based on these results, as depicted in Fig. S19 in the ESM.

As displayed in Fig. 6(a), oxygen atoms in the unit cell are categorized into three groups based on their proximity to the TM: V closest, V1, and V2. The vacancy formation energies for these oxygen vacancies are calculated in Fig. 6(b), which reveals an incremental reduction as the distance from the Mo doping site increases. Specifically, the V closest site (associated with the Mo–O octahedron) exhibits a maximum formation energy of 3.27 eV and V1 of 2.08 eV and V2 of 1.99 eV in Mo-LNO, the formation energy of oxygen vacancy increased by 130.3%, 45.5%, 40.1%, respectively. Hence, Mo anchoring to Ni sites in LNO matrix increases the oxygen release barrier, which further confirms the stability of lattice oxygen at high-temperature deep delithiation conditions.

As illustrated in Figs. 6(c)–6(f), the DOS calculations of the Ni 3d orbitals for Mo-LNO and pristine LNO reveal significant modifications in the electronic structure induced by Mo doping. Strong Ni 3d-O 2p orbital hybridization is directly evidenced by the overlapping peak profiles (Figs. 6(c) and 6(e)). In comparison to

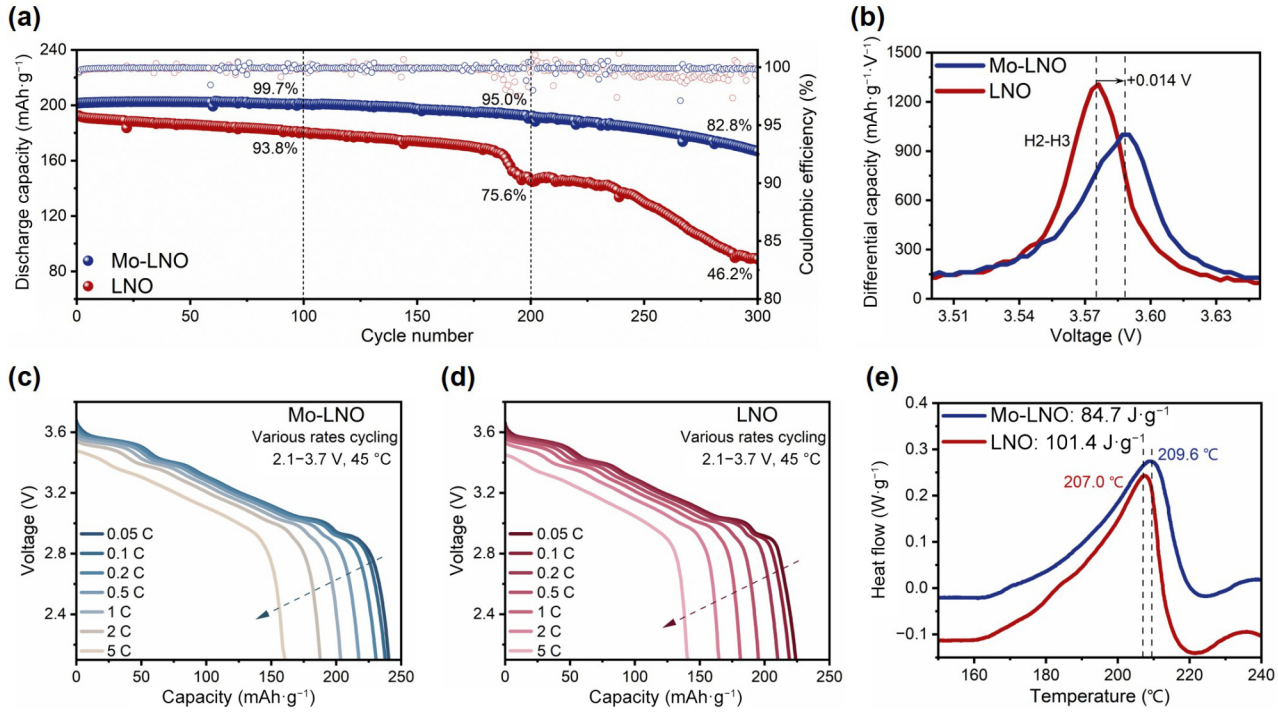

Figure 5 Comparison of the long-term cycling performance of ASSBs and thermal stability evaluation. (a) Cycling performance of ASSBs featuring Mo-LNO and LNO in the voltage range of 2.1–3.7 V at 45 °C. (b) The d*Q*/d*V* curves of ASSBs corresponding to the H2-H3 phase transitions featuring Mo-LNO and LNO cathodes. Rate capabilities of (c) Mo-LNO and (d) LNO cathodes at 45 °C. (e) The DSC curves of charged to 4.3 V Mo-LNO and LNO cathodes.

LNO, Mo-LNO exhibits the emergence of new peaks within the energy ranges of 0.2–2.0 and 4.5–6.0 eV. Notably, Mo doping enhances spin polarization of Ni 3d orbitals, leading to expansion of the t_{2g} band and increase of electronic states near the Fermi level, which collectively promotes charge transfer from O 2p to Ni e_g orbitals [53]. Furthermore, the charge density between Mo and O is greater than between Ni and O (Figs. 6(d) and 6(f)), indicating that Mo transfers more charge to the oxygen atoms, thereby forming stronger Mo–O bonding interactions. This finding is supported by the formation energies for oxygen vacancies (Fig. 6(b)), confirming that Mo-doped LNO significantly improves the electronic conductivity and bonding characteristics.

Furthermore, we calculated the diffusion energy barrier of Li^+ at 50% SOC using the Climbing Image-Nudged Elastic Band (CI-NEB) method to investigate the energy barriers associated with Li^+ migration between octahedral sites in Mo-LNO and LNO, as depicted in Figs. 6(g)–6(i). The Li^+ diffusion energy barriers for Mo-LNO and LNO are 0.80 and 1.11 eV, respectively, with a 27.9% improvement in diffusion rate of Li^+, further supporting the conclusion that Mo doping significantly enhances ionic conductivity.

In addition, regarding the structural collapse of LNO during deep delithiation, the variations in the unit cell parameters of Mo-LNO and LNO across different SOC are examined as described in Tables S3 and S4 in the ESM. The structural configurations of Mo-LNO and LNO at various SOC levels were derived by assessing all delithiation sites on the most stable structure identified in the previous step (Figs. S20 and S21 in the ESM). The findings revealed that upon doping with Mo, the *a*, *b*, and *c* axes of the unit cell expand, as supported in Rietveld refinement data (Table S2 in the ESM). As depicted in Fig. S22 in the ESM, the volume change rates for Mo-LNO (−3.84%) and LNO (−4.77%) at 83% SOC (simulating real application conditions) indicate that Mo-LNO achieves a 19.5% reduction, further supporting excellent electrochemical reversibility brought by Mo doping. Thus, the mitigation of volume contraction in Mo-LNO through enhanced grain boundary stabilization between primary particles aids in reducing the formation of mechanical cracks during charge and discharge cycles, accordingly enhances overall cycling performance under high-temperature delithiation conditions.

4 Conclusion

This study demonstrates that the incorporation of Mo^{6+} into cobalt-free LNO cathodes can facilitate half cells, coping with mechanical failure under high-temperature deep delithiation conditions. The Mo^{6+} doping preferentially enhances grain boundary interactions while mitigating structural degradation caused by anisotropic lattice contraction during deep delithiation. Additionally, the substantial increase in oxygen vacancy formation energy significantly boosts lattice oxygen stability, meanwhile the enhanced electronic states near the Fermi level and increased charge density collectively improve both electronic conductivity and bonding stability. Furthermore, the principle of high-valent Mo^{6+} doping-grain boundaries stabilization to address high-temperature delithiation challenges is proposed, which aims to enhance electronic and ionic conductivity by alleviating volume strain within the cathode and reducing partial electrochemical insulation among particles. The regulation mechanism of this study on the mechanical-electrochemical coupling behavior under deep delithiation compensates for the lack of attention to high-temperature deep delithiation scenarios in existing research, with direct implications for next-generation power battery design.

Electronic Supplementary Material: Supplementary material (preparation process for Mo-doped LNO cathode materials and

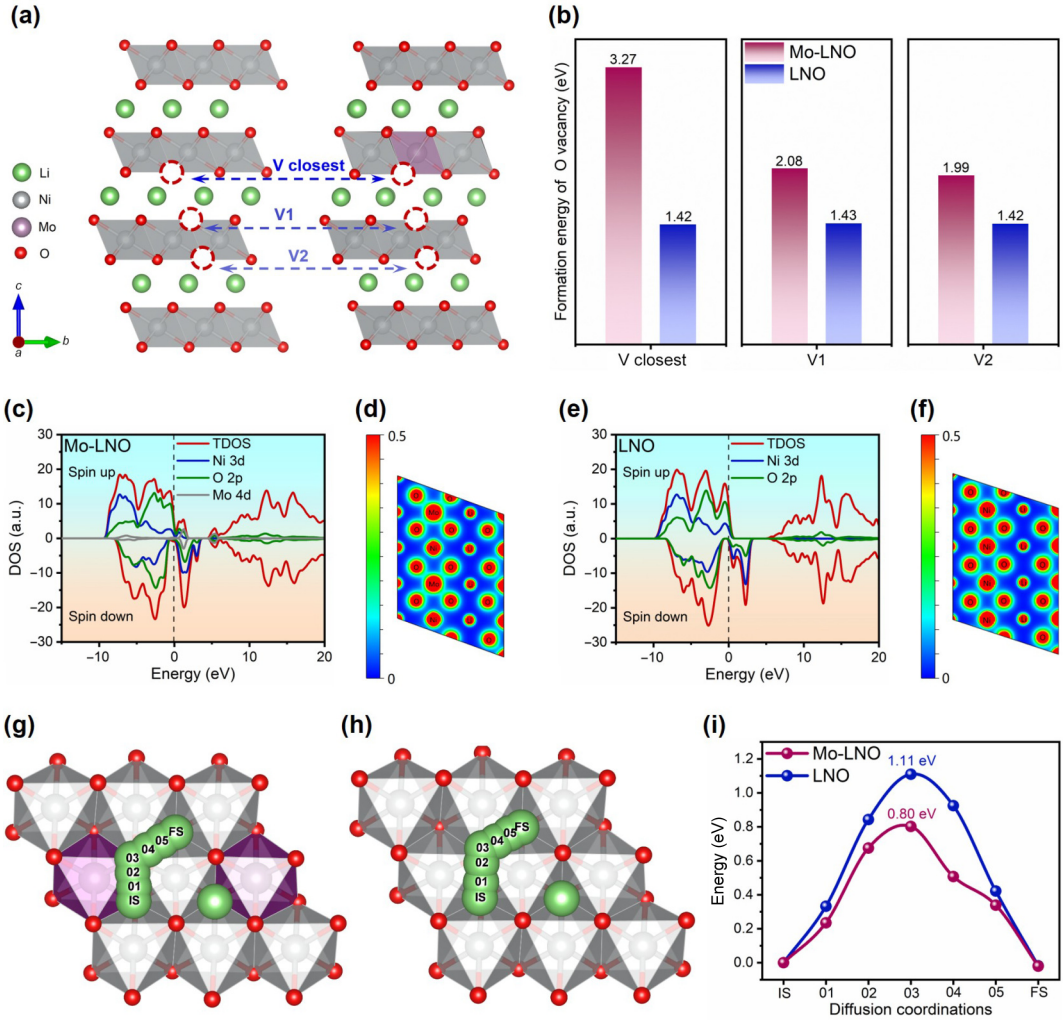

Figure 6 DFT calculation. Three schematic diagrams of (a) oxygen atom vacancies and corresponding (b) oxygen vacancy formation energies. (c) The DOS curves of Mo-LNO and corresponding (d) charge density plots. (e) The DOS curves of LNO and corresponding (f) charge density plots. Li^+ diffusion pathway diagrams of (g) Mo-LNO and (h) LNO at 50% SOC and corresponding (i) diffusion energy barriers.

coin-type half-cells; comparison of cycling performance and discharge capacity featuring undoped and Mo-doped LNO; SEM images, XRD patterns and corresponding Rietveld refinement data, and Ni 2p spectra of powder cathode materials at different doping concentrations; HAADF-STEM image of Mo-LNO and quantitative EDS line; SEM images and cross-sectional SEM images of cathodes after 100 cycles; complete dQ/dV curves and impedance spectra evolution of ASSBs; additional explanations for theoretical calculations; comparison of our work with other reported Ni-rich cathode cycles) is available in the online version of this article at https://doi.org/10.26599/NR.2025.94907901.

Data availability

All data needed to support the conclusions in the paper are presented in the manuscript and the Electronic Supplementary Material. Additional data related to this paper may be requested from the corresponding author upon request.

Acknowledgements

All the authors gratefully appreciate the financial support from the Guangxi New Energy Vehicle Laboratory Special Project (No. GuikeAA23062079) and the Special Project for Central Guidance of Local Science and Technology Development in Sichuan Province (No. 2024ZYD0302).

Declaration of competing interest

All the contributing authors report no conflict of interests in this work.

Author contribution statement

H. L.: Conceptualization, data curation, formal analysis, methodology, validation, visualization, writing – original draft, writing – review & editing. K. Q.: Formal analysis, software, validation. Y. L.: Conceptualization, writing – review & editing. C. X.: Data curation, validation. X. W. C.: Supervision. X. Y. R.: Writing – review & editing. Z. T. C.: Investigation. G. L. Z.: Funding acquisition, resources. X. L.: Conceptualization, supervision. Y. G.: Formal analysis. H. K. P.: Methodology. Y. K. G.: Visualization. C. D. L.: Project administration. B. L.: Investigation. J. W. Y.: Investigation. D. F. Z.: Supervision. T. N. T.: Conceptualization, funding acquisition, project administration, resources, supervision.

Use of AI statement

None.

References

[1] Schmuch, R.; Wagner, R.; Hörpel, G.; Placke, T.; Winter, M. Performance and cost of materials for lithium-based rechargeable automotive batteries. *Nat. Energy* **2018**, *3*, 267–278.

[2] Wang, Y.; Feng, X. N.; Peng, Y.; Zhang, F. K.; Ren, D. S.; Liu, X.; Lu, L. G.; Nitta, Y.; Wang, L.; Ouyang, M. G. Reductive gas manipulation at early self-heating stage enables controllable battery thermal failure. *Joule* **2022**, *6*, 2810–2820.

[3] Zhang, J. Z.; Wang, Y. N.; Jiang, B. B.; He, H. W.; Huang, S. B.; Wang, C.; Zhang, Y.; Han, X. B.; Guo, D. X.; He, G. N. et al. Realistic fault detection of Li-ion battery via dynamical deep learning. *Nat. Commun.* **2023**, *14*, 5940.

[4] Yoshino, A. The birth of the lithium-ion battery. *Angew. Chem., Int. Ed.* **2012**, *51*, 5798–5800.

[5] Liu, J. X.; Wang, J. Q.; Ni, Y. X.; Liu, J. D.; Zhang, Y. D.; Lu, Y.; Yan, Z. H.; Zhang, K.; Zhao, Q.; Cheng, F. Y. et al. Tuning interphase chemistry to stabilize high-voltage $LiCoO_2$ cathode material via spinel coating. *Angew. Chem., Int. Ed.* **2022**, *61*, e202207000.

[6] Park, G. T.; Namkoong, B.; Kim, S. B.; Liu, J.; Yoon, C. S.; Sun, Y. K. Introducing high-valence elements into cobalt-free layered cathodes for practical lithium-ion batteries. *Nat. Energy* **2022**, *7*, 946–954.

[7] Park, G. T.; Kim, S. B.; Namkoong, B.; Park, N. Y.; Kim, H.; Yoon, C. S.; Sun, Y. K. A new ternary Co-free layered cathode, $Li[Ni_{1-x-y}Ti_xAl_y]O_2$, for high-energy lithium-ion batteries. *Mater. Today* **2023**, *71*, 38–49.

[8] Sun, H. H.; Kim, U. H.; Park, J. H.; Park, S. W.; Seo, D. H.; Heller, A.; Mullins, C. B.; Yoon, C. S.; Sun, Y. K. Transition metal-doped Ni-rich layered cathode materials for durable Li-ion batteries. *Nat. Commun.* **2021**, *12*, 6552.

[9] Park, G. T.; Kim, S. B.; Namkoong, B.; Ryu, J. H.; Yoon, J. I.; Park, N. Y.; Kim, M. C.; Han, S. M.; Maglia, F.; Sun, Y. K. Intergranular shielding for ultrafine-grained Mo-doped Ni-rich $Li[Ni_{0.96}Co_{0.04}]O_2$ cathode for Li-ion batteries with high energy density and long life. *Angew. Chem., Int. Ed.* **2023**, *62*, e202314480.

[10] Li, C.; Liu, J. Z.; Su, Y. F.; Dong, J. Y.; Zhang, H. Y.; Wang, M.; Guan, Y. B.; Yan, K.; Liu, N.; Lu, Y. et al. Enhancing chemomechanical stability and high-rate performance of nickel-rich cathodes for lithium-ion batteries through three-in-one modification. *Energy Storage Mater.* **2025**, *74*, 103893.

[11] Geng, C. X.; Rathore, D.; Heino, D.; Zhang, N.; Hamam, I.; Zaker, N.; Botton, G. A.; Omessi, R.; Phattharasupakun, N.; Bond, T. et al. Mechanism of action of the tungsten dopant in $LiNiO_2$ positive electrode materials. *Adv. Energy Mater.* **2022**, *12*, 2103067.

[12] Bianchini, M.; Roca-Ayats, M.; Hartmann, P.; Brezesinski, T.; Janek, J. There and back again-the journey of $LiNiO_2$ as a cathode active material. *Angew. Chem., Int. Ed.* **2019**, *58*, 10434–10458.

[13] Park, N. Y.; Kim, S. B.; Kim, M. C.; Han, S. M.; Kim, D. H.; Kim, M. S.; Sun, Y. K. Mechanism of doping with high-valence elements for developing Ni-rich cathode materials. *Adv. Energy Mater.* **2023**, *13*, 2301530.

[14] Wölke, C.; Benayad, A.; Lai, T. L.; Hanke, F.; Baraldi, G.; Echeverría, M.; Esen, E.; Ayerbe, E.; Neale, A. R.; Everitt, J. et al. Single versus blended electrolyte additives: Impact of a sulfur-based electrolyte additive on electrode cross-talk and electrochemical performance of $LiNiO_2$||graphite cells. *Adv. Energy Mater.* **2024**, *14*, 2402152.

[15] Zhou, T.; Wang, H.; Wang, Y.; Jiao, P. X.; Hao, Z. M.; Zhang, K.; Xu, J.; Liu, J. B.; He, Y. S.; Zhang, Y. X. et al. Stabilizing lattice oxygen in slightly Li-enriched nickel oxide cathodes toward high-energy batteries. *Chem* **2022**, *8*, 2817–2830.

[16] Liu, T. C.; Yu, L.; Liu, J. X.; Dai, A.; Zhou, T.; Wang, J.; Huang, W. Y.; Li, L. X.; Li, M.; Li, T. Y. et al. Ultrastable cathodes enabled by compositional and structural dual-gradient design. *Nat. Energy* **2024**, *9*, 1252–1263.

[17] Bai, Z. W.; Ying, Z. H.; Zhang, F. Q.; Wang, W.; Huang, Z. Y.; Yang, T. T.; Li, W. J.; Dong, W. X.; Yan, J.; Lin, C. et al. Enabling high stability of Co-free $LiNiO_2$ cathode via a sulfide-enriched cathode electrolyte interface. *ACS Energy Lett.* **2024**, *9*, 2717–2726.

[18] Park, N. Y.; Lee, H. U.; Yu, T. Y.; Lee, I. S.; Kim, H.; Park, S. M.; Jung, H. G.; Jung, Y. C.; Sun, Y. K. High-energy, long-life Ni-rich cathode materials with columnar structures for all-solid-state batteries. *Nat. Energy* **2025**, *10*, 479–489.

[19] Liu, C.; Luo, Q. Y.; Li, L.; Wei, C. C.; Li, S. W.; Li, X.; Li, W. M.; Zhang, Z. H.; Wu, Z. K.; Jiang, Z. L. et al. Stabilization of single crystal $LiNi_{0.90}Mn_{0.05}Co_{0.05}O_2$ via ZrO_2 dual-functional coating enables superior performance for solid-state lithium battery. *Chem. Eng. J.* **2024**, *500*, 156866.

[20] Jiang, Y.; Wu, X.; Lu, G. Z.; Feng, H.; Liu, J. F.; Lv, J. X.; Geng, F. S.; Shen, M.; Hu, B. W. High-areal-capacity all-solid-state lithium batteries enabled by electronically conductive Li-deficient $LiNiO_2$ cathode. *ACS Energy Lett.* **2024**, *9*, 5529–5538.

[21] Park, N. Y.; Cho, G.; Kim, S. B.; Sun, Y. K. Multifunctional doping strategy to develop high-performance Ni-rich cathode material. *Adv. Energy Mater.* **2023**, *13*, 2204291.

[22] Yang, W.; Li, H. D.; Wang, D.; Xu, C. L.; Xiang, W.; Song, Y.; He, F. R.; Zhang, J.; Zheng, B. P.; Zhong, B. H. et al. Ta induced fine tuning of microstructure and interface enabling Ni-rich cathode with unexpected cyclability in pouch-type full cell. *Nano Energy* **2022**, *104*, 107880.

[23] Yang, W.; Bai, C. J.; Xiang, W.; Song, Y.; Xu, C. L.; Qiu, L.; He, F. R.; Zhang, J.; Sun, Y.; Liu, Y. et al. Dual-modified compact layer and superficial Ti doping for reinforced structural integrity and thermal stability of Ni-rich cathodes. *ACS Appl. Mater. Interfaces* **2021**, *13*, 54997–55006.

[24] Liu, Z. Q.; Zhang, Y. M.; Pan, S. S.; Chen, Y.; Yang, K.; Wu, S. X.; Liu, M. S.; Hu, L.; Jiang, S. C.; Wang, X. P. et al. Addressing the fundamental issues in Ni-rich cathodes: degradation mechanisms and mitigation strategies. *Energy Environ. Sci.* in press, https://doi.org/10.1039/D5EE04213E.

[25] Wang, J. J.; Yan, Y. C.; Zhao, Z. L.; Li, J. Y.; Luo, G.; Deng, D.; Peng, W. J.; Dong, M. X.; Wang, Z. X.; Yan, G. C. et al. Promoting homogeneous tungsten doping in $LiNiO_2$ through a grain boundary phase induced by excessive lithium. *Adv. Powder Mater.* **2025**, *4*, 100248.

[26] Clark, S. J.; Segall, M. D.; Pickard, C. J.; Hasnip, P. J.; Probert, M. I. J.; Refson, K.; Payne, M. C. First principles methods using CASTEP. *Z. Kristallogr. Cryst. Mater.* **2005**, *220*, 567–570.

[27] Dudarev, S. L.; Botton, G. A.; Savrasov, S. Y.; Humphreys, C. J.; Sutton, A. P. Electron-energy-loss spectra and the structural stability of nickel oxide: An LSDA+U study. *Phys. Rev. B* **1998**, *57*, 1505–1509.

[28] Grimme, S.; Antony, J.; Ehrlich, S.; Krieg, H. A consistent and accurate *ab initio* parametrization of density functional dispersion correction (DFT-D) for the 94 elements H-Pu. *J. Chem. Phys.* **2010**, *132*, 154104.

[29] Govind, N.; Petersen, M.; Fitzgerald, G.; King-Smith, D.; Andzelm, J. A generalized synchronous transit method for transition state location. *Comput. Mater. Sci.* **2003**, *28*, 250–258.

[30] Wu, F.; Liu, N.; Chen, L.; Su, Y. F.; Tan, G. Q.; Bao, L. Y.; Zhang, Q. Y.; Lu, Y.; Wang, J.; Chen, S. et al. Improving the reversibility of the H2-H3 phase transitions for layered Ni-rich oxide cathode towards retarded structural transition and enhanced cycle stability. *Nano Energy* **2019**, *59*, 50–57.

[31] Fang, Y. Y.; Su, Y. F.; Dong, J. Y.; Zhao, J. Y.; Wang, H. Y.; Li, N.; Lu, Y.; Wu, Y. J.; Li, W. B.; Yang, N. et al. Ionic-electronic dual-conductor interface engineering and architecture design in layered lithium-rich manganese-based oxides. *Carbon Energy* **2025**, *7*, e642.

[32] Kong, W. J.; Zhao, C. Z.; Shen, L.; Sun, S.; Huang, X. Y.; Xu, P.; Lu, Y.; Huang, W. Z.; Li, J. L.; Huang, J. Q. et al. Bulk/interfacial structure design of Li-rich Mn-based cathodes for all-solid-state lithium batteries. *J. Am. Chem. Soc.* **2024**, *146*, 28190–28200.

[33] Cui, Z. H.; Guo, Z. Z.; Manthiram, A. Assessing the intrinsic roles of key dopant elements in high-nickel layered oxide cathodes in lithium-based batteries. *Adv. Energy Mater.* **2023**, *13*, 2203853.

[34] Kim, Y.; Kim, H.; Shin, W.; Jo, E.; Manthiram, A. Insights into the microstructural engineering of cobalt-free, high-nickel cathodes based on surface energy for lithium-ion batteries. *Adv. Energy Mater.* **2023**, *13*, 2204054.

[35] Ding, G. Y.; Yao, M.; Li, J. H.; Yang, T. T.; Zhang, Y. D.; Liu, K. M.; Huang, X. H.; Wu, Z. H.; Chen, J. Y.; Wu, Z. Y. et al. Molten salt-assisted synthesis of single-crystalline nonstoichiometric $Li_{1+x}Ni_{1-x}O_2$ with improved structural stability. *Adv. Energy Mater.* **2023**, *13*, 2300407.

[36] Hou, Y. K.; Li, C. X.; Ren, D. S.; He, F. X.; Zhuang, K. J.; Yin, S.; Yuan, G. H.; Wang, Y. Q.; Guo, Y.; Liu, S. Y. et al. Enabling electrochemical-mechanical robustness of ultra-high Ni cathode via self-supported primary-grain-alignment strategy. *Adv. Sci.* **2023**, *10*, 2306347.

[37] Lin, L. L.; Zhang, L. H.; Fu, Z. Q.; Lou, J. T.; Gao, Z. Y.; Wu, J. R.; Li, C. L.; Han, C. P.; Zhou, D.; Wang, Z. Q. et al. Unraveling mechanism for microstructure engineering toward high-capacity nickel-rich cathode materials. *Adv. Mater.* **2024**, *36*, 2406175.

[38] Adamo, J. B.; Manthiram, A. Understanding the effects of Al and Mn doping on the H2–H3 phase transition in high-nickel layered oxide cathodes. *Chem. Mater.* **2024**, *36*, 6226–6236.

[39] Huang, H.; Zhu, H. J.; Gao, J.; Wang, J. T.; Shao, M. H.; Zhou, W. D. Grain-growth inhibitor with three-section-sintering for highly dispersed single-crystal NCM90 cubes. *Angew. Chem., Int. Ed.* **2024**, *63*, e202314457.

[40] Ovid'ko, I. A.; Sheinerman, A. G. Triple junction nanocracks in deformed nanocrystalline materials. *Acta Mater.* **2004**, *52*, 1201–1209.

[41] Park, G. T.; Yoon, D. R.; Kim, U. H.; Namkoong, B.; Lee, J.; Wang, M. M.; Lee, A. C.; Gu, X. W.; Chueh, W. C.; Yoon, C. S. et al. Ultrafine-grained Ni-rich layered cathode for advanced Li-ion batteries. *Energy Environ. Sci.* **2021**, *14*, 6616–6626.

[42] Park, G. T.; Park, N. Y.; Noh, T. C.; Namkoong, B.; Ryu, H. H.; Shin, J. Y.; Beierling, T.; Yoon, C. S.; Sun, Y. K. High-performance Ni-rich $Li[Ni_{0.9-x}Co_{0.1}Al_x]O_2$ cathodes via multi-stage microstructural tailoring from hydroxide precursor to the lithiated oxide. *Energy Environ. Sci.* **2021**, *14*, 5084–5095.

[43] Ryu, H. H.; Namkoong, B.; Kim, J. H.; Belharouak, I.; Yoon, C. S.; Sun, Y. K. Capacity fading mechanisms in Ni-rich single-crystal NCM cathodes. *ACS Energy Lett.* **2021**, *6*, 2726–2734.

[44] Wang, R. J.; Chen, J. R.; Zhang, Y. X.; Li, Z.; Cao, S.; Liu, X. L.; Hu, H.; Wu, L.; Shen, Y. Q.; Wang, X. Y. Inhibiting phase conversion and improving cyclic stability of Ni-rich layered oxide by high-valence element concentration gradient doping. *Chem. Eng. J.* **2024**, *485*, 149827.

[45] Lee, S. B.; Park, N. Y.; Park, G. T.; Kim, U. H.; Sohn, S. J.; Kang, M. S.; Ribas, R. M.; Monteiro, R. S.; Sun, Y. K. Doping strategy in developing Ni-rich cathodes for high-performance lithium-ion batteries. *ACS Energy Lett.* **2024**, *9*, 740–747.

[46] Liu, C. J.; Yi, Z. C.; Wan, J. X.; Miao, C.; Wang, Z. Y.; Wang, J. L.; Xiao, W. Nb^{5+} ions doping and Li_3PO_4 artificial layer synergetic strategy to strengthen structure, stabilize interface, and promote ions migration for high-performance Ni-rich cathode. *Chem. Eng. J.* **2025**, *503*, 158633.

[47] Cui, Z. H.; Liu, C.; Wang, F.; Manthiram, A. Navigating thermal stability intricacies of high-nickel cathodes for high-energy lithium batteries. *Nat. Energy* **2025**, *10*, 490–501.

[48] Wu, C.; Li, R.; Chen, T.; Hu, T. Z.; Wang, D. Q.; Qiu, L.; Zhong, B. H.; Wu, Z. G.; Guo, X. D. Understanding of the irreversible phase transition and Zr-doped modification strategy for a nickel-rich cathode under a high voltage. *ACS Sustain. Chem. Eng.* **2022**, *10*, 3651–3660.

[49] Tang, W. H.; Zhou, T. T.; Duan, Y.; Zhou, M. M.; Li, Z. C.; Liu, R. P. Nonflammable *in situ* PDOL-based gel polymer electrolyte for high-energy-density and high safety lithium metal batteries. *Carbon Neutralization* **2024**, *3*, 386–395.

[50] Xu, C.; Reeves, P. J.; Jacquet, Q.; Grey, C. P. Phase behavior during electrochemical cycling of Ni-rich cathode materials for Li-ion batteries. *Adv. Energy Mater.* **2021**, *11*, 2003404.

[51] Zhang, S. P.; Wu, J. Y.; Jiang, N.; Sun, H.; Yang, H. F.; Shen, L. Y.; Zhou, M. Y.; Liu, W.; Zhou, H. H.; Zhao, H. L. Surface to bulk synergetic modulation of nickel-rich $LiNi_{0.83}Co_{0.06}Mn_{0.11}O_2$ via a three-in-one approach for long-cycle lithium-ion batteries. *Adv. Energy Mater.* **2024**, *14*, 2401123.

[52] Xu, J. S.; You, J. H.; Wu, Y. S.; Zheng, R. G.; Sun, H. Y.; Liu, Y. G.; Liu, S.; Wang, Z. Y. Ultrahigh nickel cathode with microstructural refinement and intergranular coating for high-energy Li-ion batteries. *J. Energy Chem.* **2025**, *106*, 699–709.

[53] Wang, B.; Li, K.; Xu, G.; Zhang, Z. H.; Wang, X. X.; Sun, J.; Song, Y. J.; Zhang, X. D.; Liang, Y. L.; Kong, D. J. et al. Mechanically and chemically Co-robust Ni-rich cathodes with ultrahigh capacity and prolonged cycle life. *Angew. Chem., Int. Ed.* **2025**, *64*, e202502725.

This is an open access article under the terms of the Creative Commons Attribution 4.0 International License (CC BY 4.0, https://creativecommons.org/licenses/by/4.0/).

© The Author(s) 2026. Published by Tsinghua University Press.